DRAFT VERSION OCTOBER 17, 2017 Typeset using LATEX **twocolumn** style in AASTeX61

# THE ELECTROMAGNETIC COUNTERPART OF THE BINARY NEUTRON STAR MERGER LIGO/VIRGO GW170817. VII. PROPERTIES OF THE HOST GALAXY AND CONSTRAINTS ON THE MERGER TIMESCALE

P. K. Blanchard, <sup>1, 2</sup> E. Berger, <sup>1</sup> W. Fong, <sup>3, 4</sup> M. Nicholl, <sup>1</sup> J. Leja, <sup>1</sup> C. Conroy, <sup>1</sup> K. D. Alexander, <sup>1</sup> R. Margutti, <sup>4</sup> P. K. G. Williams, <sup>1</sup> Z. Doctor, <sup>5</sup> R. Chornock, <sup>6</sup> V. A. Villar, <sup>1</sup> P. S. Cowperthwaite, <sup>1</sup> J. Annis, <sup>7</sup> D. Brout, <sup>8</sup> D. A. Brown, <sup>9</sup> H.-Y. Chen, <sup>10</sup> T. Eftekhari, <sup>1</sup> J. A. Frieman, <sup>7, 11</sup> D. E. Holz, <sup>12</sup> B. D. Metzger, <sup>13</sup> A. Rest, <sup>14, 15</sup> M. Sako, <sup>8</sup> and M. Soares-Santos <sup>16, 7</sup>

and Kavli Institute for Cosmological Physics, University of Chicago, Chicago, IL 60637, USA

## ABSTRACT

We present the properties of NGC 4993, the host galaxy of GW170817, the first gravitational wave (GW) event from the merger of a binary neutron star (BNS) system and the first with an electromagnetic (EM) counterpart. We use both archival photometry and new optical/near-IR imaging and spectroscopy, together with stellar population synthesis models to infer the global properties of the host galaxy. We infer a star formation history peaked at  $\gtrsim 10$  Gyr ago, with subsequent exponential decline leading to a low current star formation rate of  $0.01 \, \mathrm{M}_\odot \, \mathrm{yr}^{-1}$ , which we convert into a binary merger timescale probability distribution. We find a median merger timescale of  $11.2^{+0.7}_{-1.4}$  Gyr, with a 90% confidence range of 6.8-13.6 Gyr. This in turn indicates an initial binary separation of  $\approx 4.5 \, \mathrm{R}_\odot$ , comparable to the inferred values for Galactic BNS systems. We also use new and archival *Hubble Space Telescope* images to measure a projected offset of the optical counterpart of  $2.1 \, \mathrm{kpc} \, (0.64 r_e)$  from the center of NGC 4993 and to place a limit of  $M_r \gtrsim -7.2$  mag on any pre-existing emission, which rules out the brighter half of the globular cluster luminosity function. Finally, the age and offset of the system indicates it experienced a modest natal kick with an upper limit of  $\sim 200 \, \mathrm{km} \, \mathrm{s}^{-1}$ . Future GW–EM observations of BNS mergers will enable measurement of their population delay time distribution, which will directly inform their viability as the dominant source of r-process enrichment in the Universe.

Keywords: gravitational waves — stars: neutron — galaxies: individual (NGC 4993)

pblanchard@cfa.harvard.edu

<sup>&</sup>lt;sup>1</sup>Harvard-Smithsonian Center for Astrophysics, 60 Garden Street, Cambridge, MA 02138, USA

<sup>&</sup>lt;sup>2</sup>NSF GRFP Fellow

<sup>&</sup>lt;sup>3</sup>Hubble Fellow

<sup>&</sup>lt;sup>4</sup>Center for Interdisciplinary Exploration and Research in Astrophysics (CIERA) and Department of Physics and Astronomy, Northwestern University, Evanston, IL 60208, USA

<sup>&</sup>lt;sup>5</sup>Department of Physics, University of Chicago, Chicago, IL 60637, USA

<sup>&</sup>lt;sup>6</sup>Astrophysical Institute, Department of Physics and Astronomy, 251B Clippinger Lab, Ohio University, Athens, OH 45701, USA

<sup>&</sup>lt;sup>7</sup>Fermi National Accelerator Laboratory, P. O. Box 500, Batavia, IL 60510, USA

<sup>&</sup>lt;sup>8</sup>Department of Physics and Astronomy, University of Pennsylvania, Philadelphia, PA 19104, USA

<sup>&</sup>lt;sup>9</sup>Department of Physics, Syracuse University, Syracuse, NY 13224, USA

<sup>&</sup>lt;sup>10</sup>Department of Astronomy and Astrophysics, University of Chicago, Chicago, IL 60637, USA

<sup>&</sup>lt;sup>11</sup>Kavli Institute for Cosmological Physics, The University of Chicago, Chicago, IL 60637, USA

<sup>&</sup>lt;sup>12</sup>Enrico Fermi Institute, Department of Physics, Department of Astronomy and Astrophysics,

<sup>&</sup>lt;sup>13</sup>Department of Physics and Columbia Astrophysics Laboratory, Columbia University, New York, NY 10027, USA

<sup>&</sup>lt;sup>14</sup>Space Telescope Science Institute, 3700 San Martin Drive, Baltimore, MD 21218, USA

<sup>&</sup>lt;sup>15</sup>Department of Physics and Astronomy, The Johns Hopkins University, 3400 North Charles Street, Baltimore, MD 21218, USA

<sup>&</sup>lt;sup>16</sup>Department of Physics, Brandeis University, Waltham, MA 02454, USA

2 Blanchard et al.

#### 1. INTRODUCTION

The recent discovery of gravitational waves (GWs) from binary black hole (BBH) mergers (Abbott et al. 2016a,b, 2017) has launched a new era of astronomy. However, realizing the full potential of GW astronomy for advancing our knowledge of the formation of compact object binaries requires the observation of electromagnetic (EM) counterparts and hence precise positions and association with specific galaxies and stellar populations. While BBH mergers are not expected to produce EM signals, a wide range of EM counterparts are expected for binary systems containing at least one neutron star (Metzger & Berger 2012).

On 2017 August 17 at 12:41:04 UT the Advanced Laser Interferometer Gravitational-Wave Observatory and Advanced Virgo interferometer (ALAV) discovered the first GW event from the inspiral and merger of two neutron stars (GW170817; LIGO Scientific Collaboration and Virgo Collaboration 2017; Abbott et al. 2017). A short burst of gammarays (GRB 170817) was independently discovered from the same sky location with a delay of about 2 s by Fermi-GBM (Goldstein et al. 2017) and INTEGRAL (Savchenko et al. 2017). About 0.5 days after the GW trigger our group used the Dark Energy Camera on the Blanco 4 m telescope to discover an optical counterpart ( $i \approx 17.48$  and  $z \approx 17.59$ mag) associated with the galaxy NGC 4993 at a distance of  $d \approx 39.5$  Mpc (Allam et al. 2017; Soares-Santos et al. 2017), which was independently discovered by Coulter et al. (2017a,b, dubbed SSS17a) and Yang et al. (2017, dubbed DLT17ck). The transient is also known as AT 2017gfo. The companion papers in this series present strong evidence that the optical counterpart is due to kilonova emission (Chornock et al. 2017; Cowperthwaite et al. 2017; Nicholl et al. 2017), with little or no contribution from a GRB afterglow due to viewing angle effects (Alexander et al. 2017; Margutti et al.

Until now, the only observational data informing the formation and evolution of binary neutron star (BNS) systems has been through studies of the Galactic population of BNS systems (e.g. Smarr & Blandford 1976; Burgay et al. 2003; Kalogera et al. 2004, 2007; Kramer & Stairs 2008) and short GRBs (Berger 2014, and references therein). Numerous open questions remain related to the initial conditions, rate, and population properties of BNS systems, as well as their eventual mergers and role in galactic r-process enrichment. For example, the distribution of delay times (i.e., the sum of the evolutionary time to form a BNS system and its time to merge) is a key output of population synthesis simulations (e.g. Voss & Tauris 2003; Belczynski et al. 2006; Dominik et al. 2012). Similarly, the observed locations of short GRBs within their hosts provides constraints on natal kicks and the possibility of globular clusters as formation sites (Fong et al. 2010; Church et al. 2011; Fong & Berger 2013).

Here, we use our follow-up observations and archival data of NGC 4993 to measure the precise location of the BNS system at the time of merger and to infer the physical properties of the host, in particular its star formation history, which serves as a proxy for the BNS merger delay time, and hence the initial binary separation. We compare these results to Galactic BNS systems and results from population synthesis models.

Throughout the Letter, we use AB magnitudes corrected for Galactic extinction, with E(B-V)=0.105 (Schlafly & Finkbeiner 2011), and the following cosmological parameters:  $H_0=67.7$  km s<sup>-1</sup> Mpc<sup>-1</sup>,  $\Omega_m=0.307$ , and  $\Omega_{\Lambda}=0.691$  (Planck Collaboration et al. 2016).

### 2. OBSERVATIONS AND ARCHIVAL DATA

## 2.1. Hubble Space Telescope (HST) Observations

As described in Cowperthwaite et al. (2017) we obtained *HST* Target-of-Opportunity observations of the optical counterpart of GW170817 on 2017 August 28 using the Advanced Camera for Surveys (ACS) with the F475W, F625W, F775W, and F850LP filters, the Wide Field Camera 3 (WFC3) IR channel with the F160W and F110W filters, and the WFC3 UVIS channel with the F336W filter (PID: 15329; PI: Berger). The data analysis is described in Cowperthwaite et al. (2017).

In Figure 1, we show a color image of NGC 4993 with an inset showing the location of the optical counterpart of GW170817 ( $m_{\rm F625W}\approx 22.9$  mag at this epoch) created using our 2017 August 28 *HST*/ACS images (F850LP, F625W, and F475W). The galaxy exhibits a smooth surface brightness profile typical of elliptical galaxies, but with a complex dust structure near the nucleus.

We also retrieved and analyzed an archival observation of NGC 4993 from 2017 April 28 using ACS/WFC with the F606W filter (PID: 14840; PI: Bellini), which allows for an assessment of an underlying source at the location of the optical counterpart. We determine the exact location of the optical counterpart in the archival image by performing astrometry relative to our HST images. The resulting astrometric uncertainty is only 0.0075'' ( $1\sigma$ ) corresponding to 0.2 pixels. No obvious source is seen at the location of the optical counterpart (Figure 1); the region is dominated by the background galaxy light. To obtain a limit on the presence of a point source we use the IRAF/psf task to create a pointspread function from the image, and the IRAF/addstar task to then inject fake point sources of varying brightness at the optical counterpart's location. We find a  $5\sigma$  upper limit of  $m_{\rm F606W} \gtrsim 26.0$  mag for a point source, corresponding to  $M_{\rm F606W} \gtrsim -7.2$  mag at the distance of NGC 4993.

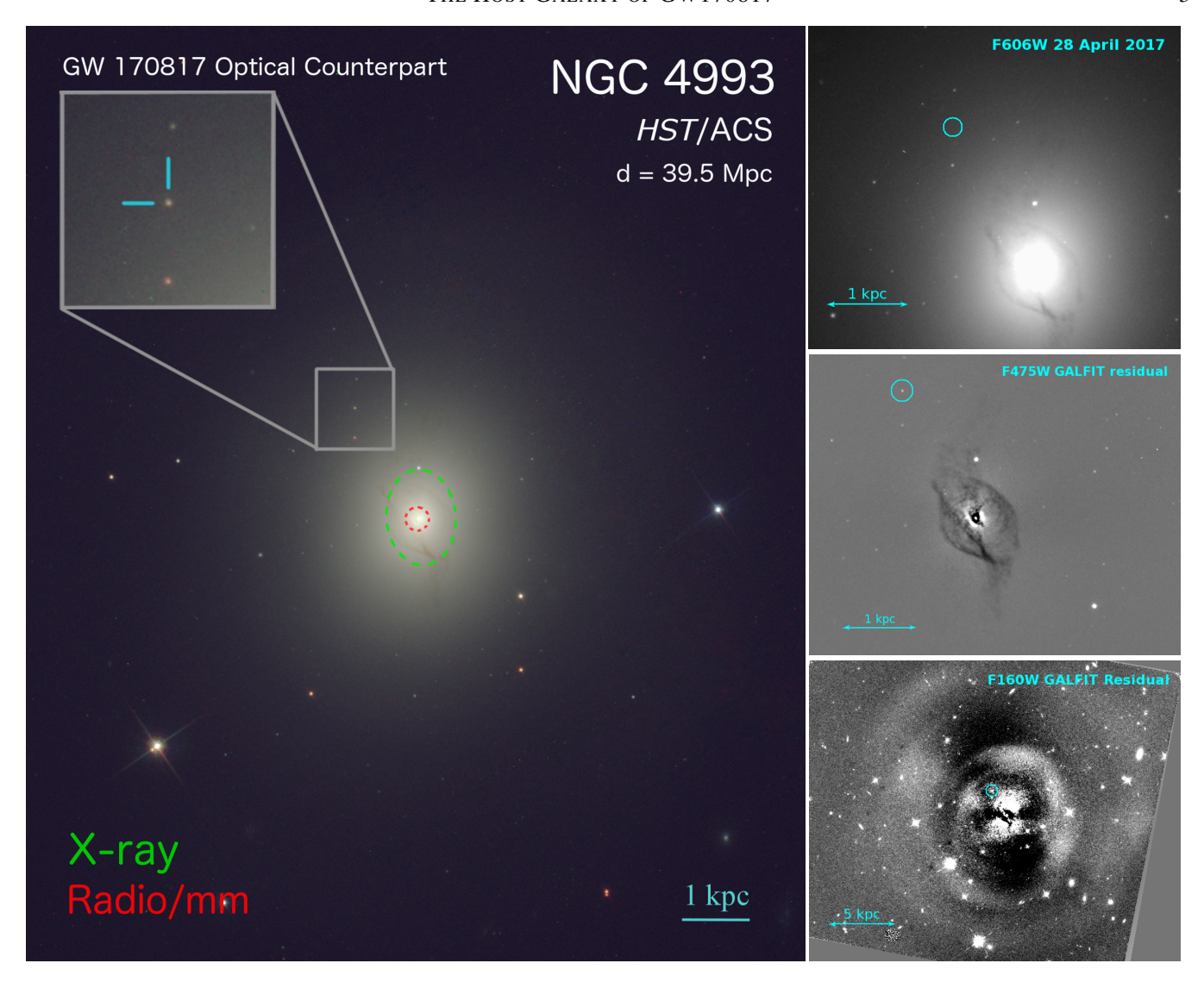


**Figure 1.** *Left*: Color image of NGC 4993 created from filtered *HST*/ACS images (F850LP, F625W, F475W). The inset shows the optical counterpart of GW170817 and the dashed green ellipse (90% confidence region) and dashed red circle ( $10\sigma$  radius for clarity) mark the locations of the X-ray (Margutti et al. 2017) and millimeter and radio sources (Alexander et al. 2017), respectively, associated with the host galaxy. *Top Right*: Archival *HST*/ACS image of NGC 4993 from 2017 April 28 exhibits no underlying point source at the position of the optical counterpart (circle) to a limit of  $M_{F606W} = -7.2$  mag. *Middle Right*: GALFIT residual image in the ACS/F475W filter showing the dust structure surrounding the nucleus. *Bottom Right*: GALFIT residual image in the WFC3/F160W filter showing the presence of concentric shells and azimuthal variations. Dust and shell structure may be indicative of past galaxy mergers. All images are aligned with North up and East to the left.

For the purpose of modeling the host galaxy spectral energy distribution (SED), we retrieved archival observations of NGC 4993, including UV and IR photometry from the GALEX, 2MASS, and WISE catalogs via the NASA/IPAC Extragalactic Database. For optical data we used deep grizy stacks from the Pan-STARRS1  $3\pi$  survey (Chambers et al. 2016; Waters et al. 2016) and performed photometry using SExtractor (Bertin & Arnouts 1996). We use the MAG\_AUTO magnitudes, which are measured using Kron apertures. The photometry is summarized in Table 1.

# 2.3. Radio and X-Ray Observations: An Active Galactic Nucleus (AGN) Origin

As described in Margutti et al. (2017) and Alexander et al. (2017), we obtained radio and X-ray observations of GW170817 with the Very Large Array (VLA), Atacama Large Millimeter/submillimeter Array (ALMA), and *Chandra*. We detect host galaxy emission in all of these observations and list the X-ray and radio fluxes in Table 1. For the X-ray emission we measure a best-fit power-law spectrum with  $\Gamma = 1.2 \pm 0.2$ , Galactic absorption with  $N_H \approx 7.84 \times 10^{20}$  cm<sup>-2</sup> (Kalberla et al. 2005), and negligible host galaxy ab-

4 Blanchard et al.

**Table 1.** X-Ray to Radio Photometry of NGC 4993

Instrument	Band	Magnitude/Flux
Chandra	2-10 keV	$1.7 \times 10^{-14}$
GALEX	FUV	> 18.86
GALEX	NUV	17.82 (0.09)
PS1	g	12.80 (0.02)
PS1	r	12.16 (0.01)
PS1	i	11.81 (0.01)
PS1	z	11.57 (0.01)
PS1	у	11.36 (0.02)
2MASS	J	10.98 (0.02)
2MASS	Н	10.82 (0.02)
2MASS	K	11.02 (0.02)
WISE	W1	11.92 (0.01)
WISE	W2	12.59 (0.01)
WISE	W3	13.70 (0.04)
WISE	W4	13.86 (0.18)
ALMA	97.5 GHz	210 (20)
VLA	15.0 GHz	295 (18)
VLA	10.0 GHz	288 (20)
VLA	9.7 GHz	250 (55)
VLA	6.0 GHz	330 (20)

NOTE—All magnitudes are given in the AB system and are corrected for Galactic extinction. Radio fluxes are in  $\mu$ Jy and the unabsorbed X-ray flux is in erg s<sup>-1</sup> cm<sup>-2</sup>.

sorption, leading to an unabsorbed flux of  $1.7 \times 10^{-14}$  erg s<sup>-1</sup> cm<sup>-2</sup> (2–10 keV), which corresponds to a luminosity of  $L_X \approx 3.2 \times 10^{39}$  erg s<sup>-1</sup>. Assuming the X-ray emission is due to star formation activity, we find a star formation rate (SFR) of SFR  $\approx 1~M_{\odot}$  yr<sup>-1</sup> using the SFR- $L_X$  relation from Grimm et al. (2003), which is about two orders of magnitude higher than the well-determined value from the broadband SED modeling in §5.

Similarly, we detect unresolved radio emission ( $\lesssim 0.2''$ , or  $\lesssim 40$  pc) from the nucleus of NGC 4993 with flux densities of about  $330\pm20~\mu\mathrm{Jy}$  at 6 GHz and  $210\pm20~\mu\mathrm{Jy}$  at 97.5 GHz. The radio-millimeter spectral index is  $\beta\approx-0.25$ , shallower than observed in star forming galaxies, but consistent with AGNs. In addition, the SFR estimated using  $L_{\nu}(6\,\mathrm{GHz})\approx 6.8\times10^{26}~\mathrm{erg}~\mathrm{s}^{-1}~\mathrm{Hz}^{-1}$  is  $\approx 0.1~M_{\odot}~\mathrm{yr}^{-1}$  (Yun

& Carilli 2002), again an order of magnitude in excess of the value from SED modeling.

Thus, the radio and X-ray emission point to the presence of a low-luminosity AGN. Using the stellar mass of NGC 4993, inferred from our SED modeling (§5), and the relation of Reines & Volonteri (2015), we infer a supermassive black hole mass of  $M_{\rm BH} \sim 10^{8.5}~\rm M_{\odot}$ . The X-ray luminosity therefore corresponds to  $\sim 10^{-7}~L_{\rm Edd}$ . For this black hole mass, the ratio of the X-ray to radio luminosity is consistent with the fundamental plane of black hole activity (Merloni et al. 2003). Furthermore, the morphology (§3) and age (§5) of NGC 4993 are typical of low-luminosity AGN hosts (Kauffmann et al. 2003).

### 2.4. Optical Spectra

During the course of obtaining optical spectra of the EM counterpart (Nicholl et al. 2017) we also obtained spectra of the host galaxy. Here, we use a spectrum obtained 1.5 days after the GW trigger with the Southern Astrophysical Research Telescope (SOAR) equipped with the Goodman High Throughput Spectrograph (Clemens et al. 2004). Observations were carried out with the 400 l/mm grating and 1" slit ( $R \sim 830$ ; see Nicholl et al. (2017) for details). We extracted the flux from NGC 4993 in an aperture of width 32 pixels around the galaxy center, corresponding to the central  $\sim$ 5". The spectra were reduced using standard IRAF routines for bias and flat-field corrections, background subtraction, and wavelength calibration. Relative flux calibration was achieved using a standard star observation on the same night; our spectral analysis is not sensitive to the absolute flux calibration.

## 3. MORPHOLOGICAL PROPERTIES OF NGC 4993

To determine the morphological properties of the host galaxy of GW170817, we measured and fit the surface brightness profile using the HST observations. We used GALFIT v3.0.5 (Peng et al. 2010) to fit the 2D surface brightness profile of NGC 4993 with a standard Sérsic function that is parameterized by the Sérsic index, n, the effective radius,  $r_e$ , and  $\mu_e$ , the surface brightness at  $r_e$ . For comparison, we also used the ellipse task in IRAF to fit isophotes to the galaxy images and then fit the resulting 1D isophotal intensity profile with a Sérsic function. In both methods, the Sérsic model is defined in such a way that  $r_e$  corresponds to the half-light radius. The best-fit Sérsic parameters from GALFIT are listed in Table 2.

In general, we find that the surface brightness profile of NGC 4993 can be well-described by a single  $n \sim 3.9$  Sérsic component with  $r_e \sim 3.3$  kpc and modest ellipticity (axis ratio  $\sim 0.85$ ). After subtracting the best-fitting GALFIT models from our data, the residual images suggest the presence of shell and asymmetric structure that are especially prominent in the F160W image (see Figure 1). There are at least

**Table 2.** Measured and Derived Properties of NGC 4993 and the Offset of the Optical Counterpart of GW170817

Property	Optical	NIR
n	3.9 (0.4)	5.1 (0.3)
$r_e$ (arcsec)	16.2 (0.7)	18.1 (1.6)
$r_e$ (kpc)	3.3 (0.1)	3.7 (0.3)
$\sigma_{\rm OT}$ (arcsec)	0.0017	0.0006
$\sigma_{\rm gal}$ (arcsec)	0.0006	0.0001
$\delta$ R.A. (arcsec)	-5.1796	-5.1730
$\delta$ Decl. (arcsec)	-8.9208	-8.9265
Offset (arcsec)	10.315 (0.007)	10.317 (0.005)
Offset (kpc)	2.125 (0.001)	2.125 (0.001)
Offset $(r_e)$	0.64 (0.03)	0.57 (0.05)
Fractional Flux	0.54	

Derived Parameters		
$A_V{}^a$	< 0.11	
$\log(\mathrm{SFR}_{100\mathrm{Myr}}/M_{\odot}\ \mathrm{yr}^{-1})$	$-2.00^{+0.44}_{-0.66}$	
$\log(M_*/M_{\odot})$	$10.65^{+0.03}_{-0.03}$	
$\log(M/M_{\odot})$	$10.90^{+0.03}_{-0.03}$	
$t_{\rm half}$ (Gyr)	$11.2^{+0.7}_{-1.4}$	
$t_{\rm age,spec}$ (Gyr)	$13.2^{+0.5}_{-0.9}$	
[Fe/H]	$0.08^{+0.02}_{-0.03}$	
[Mg/Fe]	$0.20^{+0.03}_{-0.02}$	

NOTE—Sérsic parameters are from GALFIT. Optical and NIR columns are averages of the values from the optical and NIR HST observations in several filters. [Fe/H], [Mg/Fe], and  $t_{\rm age,spec}$  are from modeling of the spectrum and all other derived properties are from modeling of the SED.

four concentric shells apparent in the F160W residual image with clear boundaries. In Figure 1, we also show the residual image in the F475W filter, zoomed to show the complex dust structure surrounding the nucleus. There is a large, approximately a few kiloparsecs, dust lane in a stretched out "s" shape, which appears to be connected to a smaller scale,  $\sim 0.1$  kpc, dust ring surrounding the brightest pixels. Both the shell and dust structures may be indicative of past galaxy mergers (e.g. Hernquist & Quinn 1988; Kormendy & Djorgovski 1989).

## 4. LOCATION OF THE OPTICAL COUNTERPART

4.1. *Offset* 

To pinpoint the location of the optical counterpart relative to its host galaxy we measure its offset from the center of NGC 4993. For each HST image in which the optical counterpart is detected, we use SExtractor to determine the uncertainty in the host galaxy center ( $\sigma_{gal}$ ) and the uncertainty in the optical counterpart location ( $\sigma_{OT}$ ), setting DEBLEND MINCONT = 0.0005 to detect the optical counterpart against the high background emission from the galaxy. We then calculate for each filter the angular and physical offset, as well as the offset normalized by the effective radius, as determined from our surface brightness profile fitting (§3); see Table 2. We find a weighted mean offset of  $2.125 \pm 0.001$ kpc, averaged over all filters. For the normalized offset we find weighted mean values in the optical and NIR bands of  $R/r_e = 0.64 \pm 0.03$  and  $0.57 \pm 0.05$ , respectively, indicating that the optical counterpart is located within the half-light radius of the galaxy. The smaller normalized offset in the NIR reflects the more extended surface brightness distribution at these wavelengths.

## 4.2. Fractional Flux

To determine the brightness of the galaxy at the location of the optical counterpart with respect to the overall host light distribution, we calculate the fraction of total galaxy light in pixels fainter than the optical counterpart position ("fractional flux"; Fruchter et al. 2006; Fong & Berger 2013; Blanchard et al. 2016); this is a commonly measured quantity in the context of GRB host galaxies. We utilize the archival HST/F606W image to measure the galaxy brightness at the optical counterpart's location, which is localized to a single pixel, and create an intensity histogram for the entire host galaxy. We consider pixels with a  $1\sigma$  brightness level above the Gaussian sky brightness distribution to be part of the host galaxy light (e.g., Fruchter et al. 2006; Fong & Berger 2013; Blanchard et al. 2016). We then determine the fraction of galaxy light in pixels fainter than the flux from the location of the optical counterpart. In this manner, we calculate a fractional flux value of 0.54. This value indicates that the galaxy brightness at the location of the optical counterpart is about average. We note that  $\approx 75-80\%$  of short GRBs occur in fainter regions of their hosts than GW170817 (Fong et al. 2017).

### 5. HOST GALAXY SED AND SPECTRAL MODELING

We model the UV to mid-IR SED of NGC 4993 using Prospector- $\alpha$ , a 14-parameter galaxy SED model (Leja et al. 2017b) that is built in the Prospector inference framework (B. Johnson et al. 2018, in preparation) and is optimized to fit UV-IR galaxy broadband photometry. Prospector- $\alpha$  uses a Bayesian Markov Chain Monte Carlo (MCMC) approach to modeling galaxy SEDs. In brief, the model fits a six-component non-parametric star formation history (SFH), a

<sup>&</sup>lt;sup>a</sup>95% upper limit

6 Blanchard et al.

two-component dust attenuation model with a flexible attenuation curve, stellar metallicity, and a flexible dust emission model powered via energy balance. Nebular line and continuum emission are added self-consistently through use of CLOUDY model grids from Byler et al. (2017). This fit additionally includes a mid-IR AGN component described in Leja et al. (2017a). SFR and stellar mass measurements from this fitting assume a Chabrier initial mass function.

In Figure 2, we show the observed SED and best-fit model. We find a low current star formation rate (averaged over the last 100 Myr) of  $\log({\rm SFR_{100\,Myr}}/M_{\odot}~{\rm yr^{-1}}) = -2.0^{+0.4}_{-0.7}$ , a total mass formed in stars of  $\log(M/M_{\odot}) = 10.90^{+0.03}_{-0.03}$ , and a stellar mass of  $\log(M_*/M_{\odot}) = 10.65^{+0.03}_{-0.03}$  (defined as the current mass in stars and stellar remnants). There is no significant dust extinction with a 95% upper limit of  $A_V < 0.11$ . Of particular interest here is the SFH, shown in eight temporal bins in Figure 2. We find an exponentially declining SFH with a peak star formation rate  $\approx 10$  Gyr ago of about  $10~M_{\odot}~{\rm yr^{-1}}$ . The SFH prior moderately favors a continuous star formation rate. The declining SFH in the posterior is thus driven by the photometry rather than the model priors.

Using the SFH, we can calculate the fraction of stars produced by a given time to obtain the stellar mass build-up history, which we also show in Figure 2. Half of the stellar mass was formed by  $11.2^{+0.7}_{-1.4}$  Gyr ago ( $t_{\rm half}$ , the half-mass assembly time), due to the high SFR at early times, and 90% was formed by  $6.8^{+2.2}_{-0.8}$  Gyr ago. We list the main physical parameters resulting from the SED modeling in Table 2.

We also model the optical spectrum of NGC 4993 with the alf stellar population synthesis modeling code (Conroy & van Dokkum 2012; Conroy et al. 2017), a two-component star formation history, the metallicity, and the abundances of 18 different elements. This complex model space is fit with MCMC techniques, with the continuum shape removed with high-order polynomials. For the present analysis we focus on three key quantities: the mass-weighted age, [Fe/H] metallicity, and [Mg/Fe], each of which is well-constrained by the data. The data and best-fit model are shown in Figure 2; the model provides an excellent fit. From the posterior distributions of the fitted parameters, we find a median mass-weighted age of  $13.2^{+0.5}_{-0.9}$  Gyr, a median metallicity of  $[Fe/H] = 0.08^{+0.02}_{-0.03}$ , and  $[Mg/Fe] = 0.20^{+0.03}_{-0.02}$ ; the age inferred here is consistent with the SED modeling results.

# 6. BNS MERGER TIMESCALE, INITIAL SEPARATION, AND KICK VELOCITY

Using the SFH determined from the SED modeling, we can infer a probability distribution for the BNS merger timescale, and hence the initial binary separation. We note that the inspiral timescale dominates over the stellar evolution timescale (which is at most tens of Myr). The cumulative stellar mass build-up history, shown in Figure 2, can there-

fore be interpreted as the integral of the merger timescale probability distribution. The inferred old age of the stellar population and the exponentially declining SFH, lead to a median merger time of  $11.2^{+0.7}_{-1.4}$  Gyr and a 90% confidence interval of 6.8-13.6 Gyr. Due to the lack of observational constraints on the intrinsic population delay time distribution (DTD), this interpretation makes the assumption that all merger times are equally probable. To check the influence of this assumption on the result, we recalculate the merger time probability distribution with the SFH weighted by a  $\tau^{-1}$  DTD (truncated at 0.1 Gyr), which results in a median merger time of  $10.3^{+1.1}_{-0.8}$  Gyr (Figure 2). While slightly shorter, the resulting merger time estimate is not significantly changed, due to the exponentially declining SFH.

The merger timescale depends on both the initial separation  $(a_0)$  and eccentricity  $(e_0)$  of the system (Peters 1964):

$$\tau_{\text{merg}}(a_0, e_0) = \frac{12}{19} \frac{c_0^4}{\beta} \int_0^{e_0} \frac{e^{29/19} [1 + (121/304)e^2]^{1181/2299}}{(1 - e^2)^{3/2}} de,$$
(1)

where

$$c_0 = \frac{a_0(1 - e_0^2)}{e_0^{12/19}} [1 + (121/304)e_0^2]^{-870/2299}$$
 (2)

and  $\beta$  is a constant related to the total and reduced mass. Here we assume nominal neutron star masses of 1.4  $M_{\odot}$  since at the time of writing the measured neutron star masses from the GW data were not publicly available. We can therefore convert our inferred median and 90% confidence merger timescale to  $a_0$  as a function of  $e_0$ ; see Figure 3. For  $e_0 \lesssim 0.5$  we find  $a_0 \approx 3.9-4.7$  R $_{\odot}$  with a median of  $\approx 4.5$  R $_{\odot}$ . However, if the initial eccentricity of the system was large ( $e_0 \gtrsim 0.8$ ), then the initial separation could be tens of R $_{\odot}$ .

In Figure 3, we also show the initial separations and eccentricities for the simulated population of BNS systems from Dominik et al. (2012) using their standard model (sub-model A) with solar metallicity, appropriate for NGC 4993. The population has an overdensity roughly centered along the contour for  $\sim 100$  Myr, though there is considerable spread in the initial separations and thus timescales for a given eccentricity. At low eccentricity ( $e_0 \lesssim 0.2$ ) the distribution of separations peaks at about a factor of 2-3 less than the separation of the progenitor of GW170817, though even at these eccentricities the spread is large. Interestingly, the region of  $a_0-e_0$  parameter space for the progenitor of GW170817 is mid-range compared to the Galactic BNS systems.

Combining the location of GW170817 within its host and the merger timescale probability distribution, we can assess the velocity imparted to the system due to a natal kick. There are several unknown factors such as the formation location of the system, the fact that we can only measure a projected

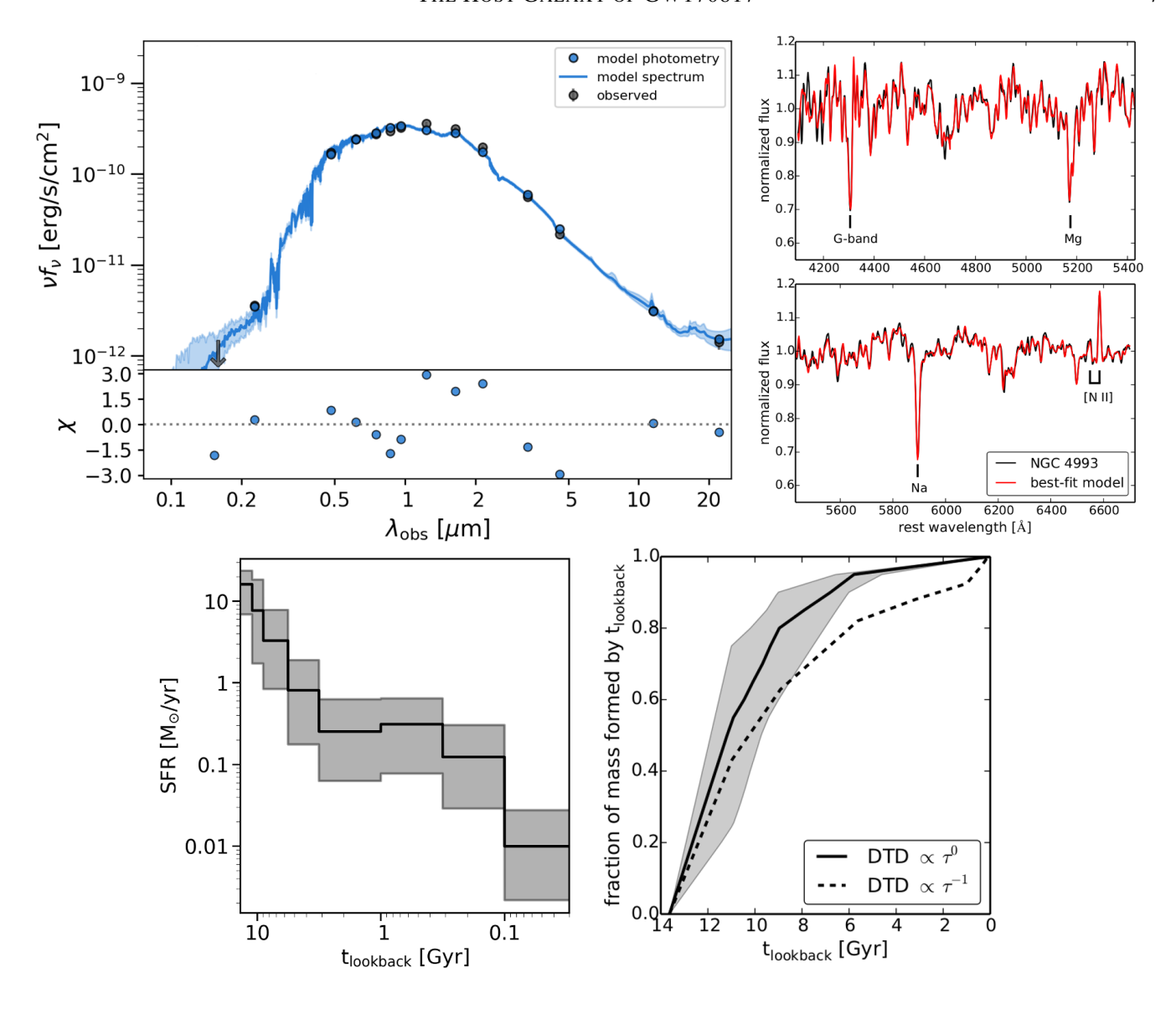


**Figure 2.** Top Left: Observed SED of NGC 4993 (black circles) with the best-fit Prospector- $\alpha$  model (blue line; shaded region marks the 16th–84th percentile range). Top Right: Observed optical spectrum of the nucleus of NGC 4993 (black line) with the best-fit spectral model (red line). Bottom Left: The star formation history of NGC 4993 from the best fit SED model (black line; shaded region marks the 16th–84th percentile range). The SFH exhibits an overall exponential decline, with a very low present-day star formation rate. Bottom Right: Stellar mass build-up history (solid black line; shaded region marks the 16th–84th percentile range) as inferred from the SFH. We find that 50% of the stellar mass was formed by  $11.2^{+0.7}_{-1.4}$  Gyr ago and 90% was formed by  $6.8^{+2.2}_{-0.8}$  Gyr ago. Without prior knowledge of the intrinsic DTD of BNS mergers, the build-up history represents a proxy for the merger time probability distribution. The dashed black line represents the resulting merger time probability distribution obtained by weighting the SFH with a  $\tau^{-1}$  DTD truncated at 0.1 Gyr, which slightly shifts the distribution toward shorter merger times. The uncertainty region is similar to that for the solid line.

offset, and the exact gravitational potential of the host galaxy. However, given the long merger timescale and the measured location within the host's half-light radius, it is most likely that any natal kick was not strong enough to unbind the binary from the host on an escaping trajectory. Assuming the progenitor system was born near or within its current small offset, we can use the central stellar velocity dispersion  $(\sigma_*)$  to set an upper limit on the kick velocity. The velocity disper-

sion is only marginally resolved in the host spectrum, yielding a nominal value of  $\sigma_* \approx 150 \text{ km s}^{-1}$  from the model fitting. As the dispersion is less than the instrumental resolution, we consider the instrumental resolution to be a conservative upper limit on the velocity dispersion and therefore the kick velocity, which yields  $v_{kick} \lesssim 200 \text{ km s}^{-1}$ . This value is within the range of observed and simulated velocity distri-

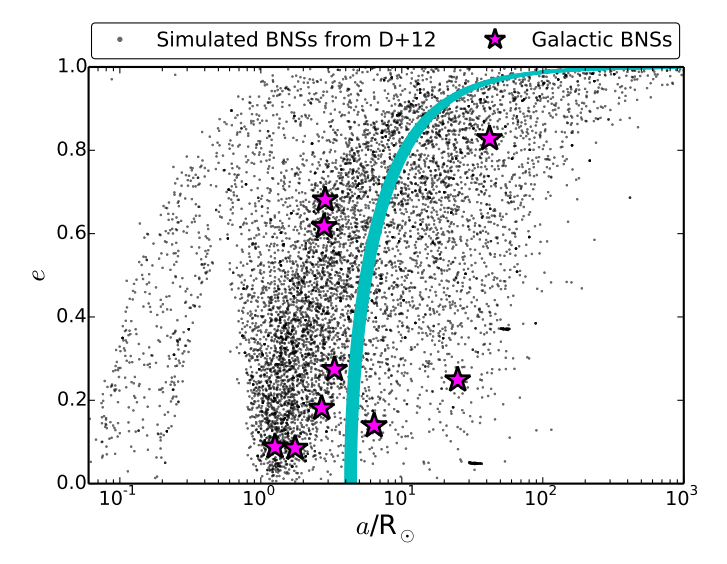


**Figure 3.** Initial separation versus eccentricity plane with a shaded contour (cyan) representing the 90% confidence interval for the merger timescale of the progenitor of GW170817. Magenta stars and black points represent the current *a* and *e* for Galactic BNS systems (Voss & Tauris 2003; Wong et al. 2010, and references therein) and a population of simulated BNS systems from Dominik et al. (2012), respectively.

butions for Galactic BNS systems (Wong et al. 2010; Tauris et al. 2017).

Finally, we assess the possibility of a globular cluster origin for the progenitor of GW170817 (e.g., Lee et al. 2010). We compare the limit on an underlying point source at the location of the progenitor ( $\gtrsim$  -7.2 mag) to the globular cluster luminosity function (GCLF) for giant elliptical galaxies, which peaks at  $M_V \approx$  -7.4 mag, with the brightest observed system at  $M_V \approx$  -10 mag (Harris et al. 1991). Strader et al. (2006) found that the luminosity at the peak of the GCLF remains the same regardless of galaxy size for elliptical galaxies. Thus, the archival limit rules out the brighter half of the GCLF. Additional, deeper observations will be needed to definitively rule out a globular cluster at the position of the optical counterpart.

## 7. CONCLUSIONS

We presented new and archival data for NGC 4993, the host galaxy of the first BNS merger discovered through GW emission, and the first with an EM counterpart. Using these data we investigated the location of the progenitor within its host, determined critical properties of the galaxy and its stellar population, and placed constraints on the merger timescale, initial separation, and kick velocity of the BNS system. Our key findings are:

• The host galaxy of GW170817 is an elliptical galaxy that is well-described by a  $n \approx 3.9$  Sérsic profile in

the optical, but with significant fine shell structure in the NIR indicative of past galaxy mergers. We detect NGC 4993 with X-ray and radio luminosities that suggest the presence of a weak AGN.

- The offset of the BNS system from the nucleus of NGC 4993 is 2.1 kpc, with a normalized offset of 0.64 in the optical and 0.57 in the NIR, indicating that the merger took place within the host's half-light radius. The fractional flux value is 0.54, consistent with this conclusion.
- From modeling the UV to MIR SED we find an exponentially declining SFH, with a median stellar population age of  $11.2^{+0.7}_{-1.4}$  Gyr. The present-day SFR is low,  $\approx 0.01~M_{\odot}~\text{yr}^{-1}$ .
- The median merger timescale is therefore  $11.2^{+0.7}_{-1.4}$  Gyr for the progenitor of GW170817, with a 90% probability the BNS system formed between 6.8-13.6 Gyr ago. Assuming a circular orbit and equal neutron star masses of  $1.4~M_{\odot}$ , this corresponds to an initial separation of  $3.9-4.7~R_{\odot}$  with a median of  $4.5~R_{\odot}$ ; for large initial eccentricity the separation could be tens of  $R_{\odot}$ .
- Given the long merger timescale and small projected offset, we conclude that the binary system experienced at most a modest natal kick, with an upper limit of 200 km s<sup>-1</sup>.

This Letter demonstrates the utility of detailed host galaxy studies for inferring the properties of BNS systems. Studying the host galaxies of future BNS mergers discovered by ALAV and localized by EM follow-up will allow for an observational measurement of the population DTD, a key parameter that informs the viability of BNS mergers as the dominant source of *r*-process enrichment in the Universe. Comparison of the DTD as well as separations, natal kicks, and merger rates with population synthesis models will also yield great insight into uncertain phases, such as the common envelope phase, of massive star binary evolution.

The Berger Time-Domain Group at Harvard is supported in part by the NSF through grants AST-1411763 and AST-1714498, and by NASA through grants NNX15AE50G and NNX16AC22G. P.K.B. is grateful for support from the National Science Foundation Graduate Research Fellowship Program under grant No. DGE1144152. D.A.B. is supported by NSF award PHY-1707954. This research has made use of the NASA/IPAC Extragalactic Database (NED), which is operated by the Jet Propulsion Laboratory, California Institute of Technology, under contract with the National Aeronautics and Space Administration. Some of the data presented in this

Letter were obtained from the Mikulski Archive for Space Telescopes (MAST). STScI is operated by the Association of Universities for Research in Astronomy, Inc., under NASA contract NAS5-26555. Support for MAST for non-HST data is provided by the NASA Office of Space Science via grant NNX09AF08G and by other grants and contracts.

Facilities: HST (ACS, WFC3), SOAR, VLA, ALMA, CXO

## **REFERENCES**

Abbott, B. P., Abbott, R., Abbott, T. D., et al. 2016a, Physical Review Letters, 116, 241103 —. 2016b, Physical Review Letters, 116, 061102 —. 2017, Physical Review Letters, 118, 221101 Abbott et al. 2017, Physical Review Letters, Submitted Alexander et al. 2017, ApJL, in press Allam et al. 2017, GRB Coordinates Network, 21530 Belczynski, K., Perna, R., Bulik, T., et al. 2006, ApJ, 648, 1110 Berger, E. 2014, ARA&A, 52, 43 Bertin, E., & Arnouts, S. 1996, A&AS, 117, 393 Blanchard, P. K., Berger, E., & Fong, W.-f. 2016, ApJ, 817, 144 Burgay, M., D'Amico, N., Possenti, A., et al. 2003, Nature, 426, Byler, N., Dalcanton, J. J., Conroy, C., & Johnson, B. D. 2017, ApJ, 840, 44 Chambers, K. C., Magnier, E. A., Metcalfe, N., et al. 2016, ArXiv e-prints, arXiv:1612.05560 [astro-ph.IM] Chornock et al. 2017, ApJL, in press Church, R. P., Levan, A. J., Davies, M. B., & Tanvir, N. 2011, MNRAS, 413, 2004 Clemens, J. C., Crain, J. A., & Anderson, R. 2004, in Proc. SPIE, Vol. 5492, Ground-based Instrumentation for Astronomy, ed. A. F. M. Moorwood & M. Iye, 331 Conroy, C., & van Dokkum, P. 2012, ApJ, 747, 69 Conroy et al. 2017, Submitted Coulter et al. 2017a, Science, Submitted -.. 2017b, GRB Coordinates Network, 21529 Cowperthwaite et al. 2017, ApJL, in press Dominik, M., Belczynski, K., Fryer, C., et al. 2012, ApJ, 759, 52 Fong, W., & Berger, E. 2013, ApJ, 776, 18 Fong, W., Berger, E., & Fox, D. B. 2010, ApJ, 708, 9 Fong et al. 2017, ApJL, in press Fruchter, A. S., Levan, A. J., Strolger, L., et al. 2006, Nature, 441,

Goldstein et al. 2017, ApJL, Submitted

S. 1991, ApJS, 76, 115

Grimm, H.-J., Gilfanov, M., & Sunyaev, R. 2003, MNRAS, 339,

Harris, W. E., Allwright, J. W. B., Pritchet, C. J., & van den Bergh,

```
Hernquist, L., & Quinn, P. J. 1988, ApJ, 331, 682
Kalberla, P. M. W., Burton, W. B., Hartmann, D., et al. 2005,
  A&A, 440, 775
Kalogera, V., Belczynski, K., Kim, C., O'Shaughnessy, R., &
  Willems, B. 2007, PhR, 442, 75
Kalogera, V., Kim, C., Lorimer, D. R., et al. 2004, ApJL, 614, L137
Kauffmann, G., Heckman, T. M., Tremonti, C., et al. 2003,
  MNRAS, 346, 1055
Kormendy, J., & Djorgovski, S. 1989, ARA&A, 27, 235
Kramer, M., & Stairs, I. H. 2008, ARA&A, 46, 541
Lee, W. H., Ramirez-Ruiz, E., & van de Ven, G. 2010, ApJ, 720,
Leja, J., Johnson, B. D., Conroy, C., & van Dokkum, P. 2017a,
  ArXiv e-prints, arXiv:1709.04469
Leja, J., Johnson, B. D., Conroy, C., van Dokkum, P. G., & Byler,
  N. 2017b, ApJ, 837, 170
LIGO Scientific Collaboration and Virgo Collaboration. 2017,
  GRB Coordinates Network, 21509
Margutti et al. 2017, ApJL, in press
Merloni, A., Heinz, S., & di Matteo, T. 2003, MNRAS, 345, 1057
Metzger, B. D., & Berger, E. 2012, ApJ, 746, 48
Nicholl et al. 2017, ApJL, in press
Peng, C. Y., Ho, L. C., Impey, C. D., & Rix, H.-W. 2010, AJ, 139,
  2097
Peters, P. C. 1964, Physical Review, 136, 1224
Planck Collaboration, Ade, P. A. R., Aghanim, N., et al. 2016,
  A&A, 594, A13
Reines, A. E., & Volonteri, M. 2015, ApJ, 813, 82
Savchenko et al. 2017, ApJL, Submitted
Schlafly, E. F., & Finkbeiner, D. P. 2011, ApJ, 737, 103
Smarr, L. L., & Blandford, R. 1976, ApJ, 207, 574
Soares-Santos et al. 2017, ApJL, in press
Strader, J., Brodie, J. P., Spitler, L., & Beasley, M. A. 2006, AJ,
  132, 2333
Tauris, T. M., Kramer, M., Freire, P. C. C., et al. 2017, ApJ, 846,
  170
Voss, R., & Tauris, T. M. 2003, MNRAS, 342, 1169
Waters, C. Z., Magnier, E. A., Price, P. A., et al. 2016, ArXiv
  e-prints, arXiv:1612.05245 [astro-ph.IM]
Wong, T.-W., Willems, B., & Kalogera, V. 2010, ApJ, 721, 1689
Yang et al. 2017, GRB Coordinates Network, 21531
```

Yun, M. S., & Carilli, C. L. 2002, ApJ, 568, 88